

Heterogeneous Creep Deformations and Correlation to Microstructures in Fe-30Cr-3Al Alloys Strengthened by an Fe₂Nb Laves Phase



BENJAMIN SHASSERE, YUKINORI YAMAMOTO, JONATHAN POPLAWSKY, WEI GUO, and SUDARSANAM SURESH BABU

A new Fe-Cr-Al (FCA) alloy system has been developed with good oxidation resistance and creep strength at high temperature. The alloy system is a candidate for use in future fossil-fueled power plants. The creep strength of these alloys at 973 K (700 °C) was found to be comparable with traditional 9 pct Cr ferritic–martensitic steels. A few FCA alloys with general composition of Fe-30Cr-3Al-.2Si-*x*Nb (*x* = 0, 1, or 2) with a ferrite matrix and Fe₂Nb-type Laves precipitates were prepared. The detailed microstructural characterization of samples, before and after creep rupture testing, indicated precipitation of the Laves phase within the matrix, Laves phase at the grain boundaries, and a 0.5 to 1.5 μm wide precipitate-free zone (PFZ) parallel to all the grain boundaries. In these alloys, the areal fraction of grain boundary Laves phase and the width of the PFZ controlled the cavitation nucleation and eventual grain boundary ductile failure. A phenomenological model was used to compare the creep strain rates controlled by the effects of the particles on the dislocations within the grain and at grain boundaries. (The research sponsored by US-DOE, Office of Fossil Energy, the Crosscutting Research Program).

DOI: 10.1007/s11661-017-4274-8

© The Minerals, Metals & Materials Society and ASM International 2017

I. INTRODUCTION

A. Motivation

THE challenge for the continued use of fossil energy is to reduce carbon emissions. The main source of CO₂ is electricity generation, which accounts for 30 pct of emissions in the United States.^[1] Fossil-fueled power plants can reduce emissions by improving efficiency through increasing steam temperature and pressure. It

has been demonstrated by Abe,^[2] that increasing the steam temperature and pressure from 811 K (538 °C) and 24.1 MPa, to 923 K (650 °C) and 34.3 MPa, respectively, can increase the energy conversion efficiency by 6.5 pct, which could potentially reduce CO₂ emission. For these demanding conditions, a variety of steels have been developed with a host of alloy design and heat treatment strategies. Traditionally, the family of 9 pct Cr (in wt pct) Creep Strength Enhanced Ferritic (CSEF) steels used in fossil-fueled power plants today have a tempered martensitic matrix with a fine distribution of Cr-rich alloy carbides. However, with an increase in temperature, the creep resistance of the 9 pct Cr steel, Grade 91 (9Cr 1Mo major additions), steel welds are found to be inferior when compared to the base metal. There are reports of failures of these steel weldments after a few years in service.^[3–8] These failures have been attributed to the formation of soft ferrite regions in the Fine Grain Heat-Affected Zone (FGHAZ) (Type IV region) that occurred when the materials were welded. The formation of the soft ferrite was attributable to incomplete dissolution of M₂₃C₆ carbides during typical heat-affected zone (HAZ) thermal cycles.^[6–8] If the operational temperatures and pressures are to be realized, it is necessary to create an alloy system that eliminates these types of failures.

In recent years, there has been a development of a Grade 92 steel with additional strengthening from an

BENJAMIN SHASSERE and SUDARSANAM SURESH BABU are with the Department of Mechanical, Aerospace, and Biomedical Engineering, The University of Tennessee, Knoxville, TN 37996. Contact e-mail: bashassere21@gmail.com YUKINORI YAMAMOTO, JONATHAN POPLAWSKY, and WEI GUO are with the Materials Science and Technology Division, Oak Ridge National Laboratory, Oak Ridge, TN 37831.

This manuscript has been authored by UT-Battelle, LLC under Contract No. DE-AC05-00OR22725 with the U.S. Department of Energy. The United States Government retains and the publisher, by accepting the article for publication, acknowledges that the United States Government retains a non-exclusive, paid-up, irrevocable, world-wide license to publish or reproduce the published form of this manuscript, or allow others to do so, for United States Government purposes. The Department of Energy will provide public access to these results of federally sponsored research in accordance with the DOE Public Access Plan (<http://energy.gov/downloads/doe-public-access-plan>).

Manuscript submitted April 11, 2017.

Article published online August 7, 2017

intermetallic Laves phase by the addition of tungsten (W). Abe,^[9] has shown the effect of the fine (<100 nm) precipitation of Fe₂X (X: W, Nb, *etc.*) Laves phase. While aging of the Grade 92 steel during creep, Laves phase precipitated on the prior austenite grain boundaries and martensite block boundaries, which reduced the creep rate when compared to traditional Grade 91 steel. With the presence of traditional M₂₃C₆ carbides within the matrix, potential for Type IV cracking during creep is still relevant. There has been simultaneous development of carbon lean Fe-Cr alloys for Solid Oxide Fuel Cells for high temperature creep resistance. Several variations have been created with controlled additions of W, Nb, Si, Mo, and Co, which all tend to form an intermetallic Fe₂X Laves phase. In these alloys, the microstructure remains fully ferritic from solidification to room temperature. On aging of these carbon lean alloys, Laves phase precipitates from the ferrite matrix, providing strengthening. Shibuya *et al.*,^[10] have developed a 15Cr-1Mo-2Co-6W-V-Nb (in wt pct) alloy, which relies on the precipitation of Fe₂Nb intermetallics and M₂₃C₆ carbides. The researchers showed that this alloy system performed as well as conventional Grade 92 ferritic steels. However, this alloy contained the M₂₃C₆ carbide, which has been shown to coarsen rapidly during thermal cycles typical of welding and service aging. At the same time, Kuhn *et al.*,^[11] developed a 22Cr-W-Nb alloy, strengthened only by Fe₂Nb and Fe₂W intermetallic Laves phase. In this alloy system, the intermetallic compounds did not coarsen rapidly (coarsening rate of 10⁻²⁸ m³ s⁻¹); however, the creep strength was low when compared to conventional Grade 91 steels. The 10,000 hours rupture stress at 973 K (700 °C) for the Grade 91 steels is approximately 40 MPa while that for the 22Cr alloys is approximately 20 MPa. Another challenge for these fully ferritic alloys is the formation of sigma phase. Sigma phase is an intermetallic of Fe and Cr, and is found to be detrimental to the creep rupture properties. It should be noted when comparing the fully ferritic alloys to the Grade 91 steels that there are differences in service temperature. The service temperatures for the Grade 91 steels are between 823 K and 923 K (550 °C and 650 °C). The service temperature of the Fe-Cr ferritic alloys would need to be maintained above the sigma phase solution temperature. In the current research alloys, the sigma phase solution temperature is approximately 923 K (650 °C). The alloy is expected to be free of sigma phase at a service temperature of 973 K (700 °C). With good creep resistance and excellent steam oxidation resistance, these alloys are good candidates for components in modern power plants. This research focuses on the Fe-30Cr-3Al fully ferritic alloys, with increased Nb contents, and correlates the microstructure to creep properties in the alloy system.

B. Creep Response of the Fe-Cr-Al Alloy

The creep rupture curves of four Iron–Chromium–Aluminum (FCA) alloys that have varying niobium concentrations have been published elsewhere.^[12] The results from that investigation are as follows. The alloy lean in

Nb failed quickly; 1.4 hours. This is expected, because there is a lack of strengthening precipitates. When 1 wt pct Nb was added, the sample failed after 138 hours (minimum creep rate, 1.75 × 10⁻⁶ pct s⁻¹). The creep performance improves with an additional 1 wt pct Nb, which failed after 1760 hours (1.47 × 10⁻⁷ pct s⁻¹). However, with an addition of 0.1 wt pct Zr to the 2 wt pct Nb, the creep performance was reduced and failed after 1330 hours (9.23 × 10⁻⁸ pct s⁻¹). The results lead to a conclusion that the addition of Nb improves the creep rupture properties. However, it is necessary to understand the microstructure of the alloys before, during, and after creep rupture, such that the data can be rationalized based on the microstructural evolution over time.

The time to failure and creep rates can be compared to existing literature. Chiu and Lin,^[13] provided results from various alloys, *i.e.*, Crofer 22H, a 0.5Nb, and 1.94W modified 22Cr fully ferritic Laves-strengthened alloy. The author presented creep curves in a range of temperatures from 923 K to 1073 K (650 °C to 800 °C). The time to failure of the literature sample with creep condition 73 MPa and 973 K (700 °C) was 1100 hours. This result is in the same order of magnitude of the results from the FCA-2Nb alloy, confirming the expected performance of a Laves phase-strengthened alloy.

To obtain an understanding of the creep mechanisms to be able to correlate with the microstructures, instantaneous strain rates were calculated from the secondary creep or “steady state” regime. A differential calculation was applied to the raw creep curves, but because of the noise in the raw data the differential curves were rather noisy and the plot of the data revealed no discernable trend. To eliminate the noise, the creep curves were digitized and smoothed to arrive at strain rate curves (see Figure 1(a)). The curves were digitized using an Igor Pro macro. Care was taken to make sure the original creep curve shape and magnitudes were conserved during digitization. Figure 1(b) shows the calculated strain rates with time. The FCA-1Nb curve does not show a reduction in creep rate before the onset of tertiary creep and exhibits continued acceleration of creep rate. This suggests that the microstructure did not yield good creep resistance at 973 K (700 °C) and 70 MPa. On the other hand, the 2 wt pct Nb-containing alloy did show the typical strain rate *vs* time curve observed in typical precipitate-strengthened steels. In addition, the FCA-2Nb sample had a short transition of accelerated creep rate during the tertiary creep regime when compared with other precipitate-strengthened steels like Grade 91.^[9,14] The range of tertiary creep regime of the FCA alloys was only 100 to 200 hours. In comparison, the tertiary creep regime in Grade 91 steels can last well over 1000 hours. The acceleration of deformation in the tertiary stage was unexpected behavior, and this paper will attempt to understand this behavior. The Zr-containing alloy started out with a lower creep rate and approached the minimum creep rate faster than other alloys. This would suggest changes in microstructure initially providing high creep resistance, but transitioned to a condition that led to rapid failure. The above unexpected creep rate transients

formed the motivation for the current research paper. This paper examines the microstructure of the FCA alloys with aging and after creep rupture. The microstructure analysis is then used to correlate the creep properties and failure mechanisms to the observed microstructures.

II. EXPERIMENTAL APPROACH

The chemical compositions of the FCA ferritic alloys are shown in Table I. Four model alloys were made with the base alloy consisting of Fe, Cr, Al, and a small addition of Si. Traditionally, carbon and boron are added for strengthening and precipitation; however, these were not added to the alloy because our alloy design strategy is to avoid carbide or boride formation. The first model alloy did not contain Nb, to act as a control sample with a 100 pct ferritic microstructure. Nb was added to three of the alloys to induce Laves phase formation and to enhance creep strength. Zr was

added to the fourth alloy to promote additional Laves phase development, and as a grain refiner.

A. Alloys and Heat Treatment

All the alloys were vacuum-arc melted and drop cast at the Oak Ridge National Laboratory. Heat treatment temperatures were designed using thermodynamic calculations (using JMatPro[®], general steels database) and were specifically chosen to lead to complete dissolution of Laves phases. Because of the differences in Nb concentration, the heat treatment conditions were modified for the various alloys. The FCA-0Nb and FCA-1Nb alloys were homogenized at 1573 K (1300 °C) for 1 hour then cooled to room temperature. A hot rolling sequence totaling 60 pct reduction with a rolling preheat of 1473 K (1200 °C) was performed. Hot rolling was followed by warm rolling with a 75 pct reduction sequence using a preheat temperature of 573 K (300 °C). Finally, a solution heat treatment was performed after rolling; 30 minutes at 1373 K (1100 °C) plus five minutes at 1473 K (1200 °C). The last step was performed to dissolve any residual Laves phase but limit grain growth. The FCA-2Nb and FCA-2Nb-0.1Zr were subjected to a different heat treatment because of the increased Nb content. After arc melting and drop casting, the alloys were homogenized at 1573 K (1300 °C) for 1 hour. The alloys were hot forged with a preheat temperature of 1573 K (1300 °C) to a 67 pct thickness reduction, then hot rolled with a preheat temperature of 1573 K (1300 °C) further reducing the thickness by 70 pct. The post rolling solution heat treatment was ten minutes at 1573 K (1300 °C). Samples extracted from the FCA-1Nb and FCA-2Nb plates were subjected to an aging study. The samples were aged at 973 K, 1073 K, and 1173 K (700 °C, 800 °C, and 900 °C) for two times; 168 hours and 1008 hours. The aging study allowed the understanding of the kinetics of the Laves phase growth with the comparison of the microstructure of samples subjected to creep rupture testing.

B. Creep Testing

Due to a limitation of available materials, creep tests were performed using sub-sized samples, compared to ASTM standards.^[15,16] It should be noted that there is a possibility of a size effect on the creep properties due to specimen size limitations since large grains were observed. [If the sample size is on the scale of the grain size, and grain boundary creep is the dominating mechanism, the samples would not exhibit true bulk creep deformation.^[17,18]] Therefore, the data and discussions on microstructural effects are considered

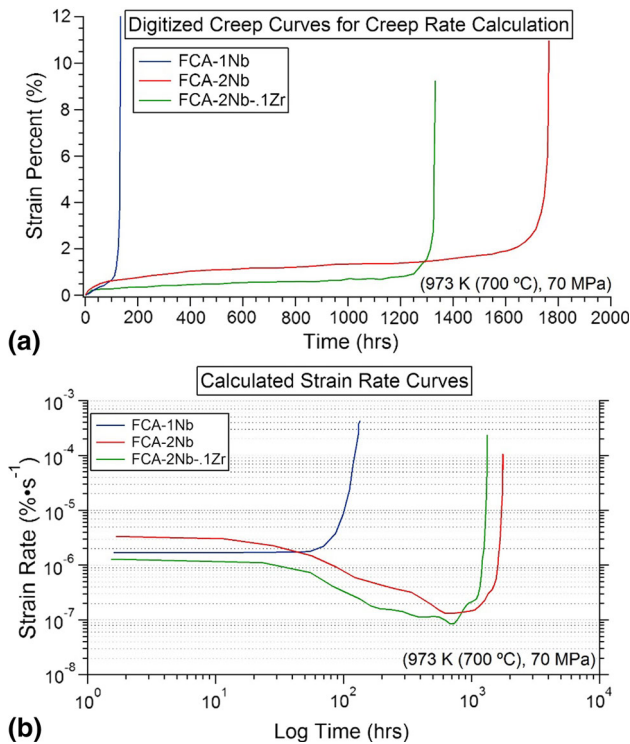


Fig. 1—(a) Digitized creep curves from original data, the creep curves are smoothed to calculate creep rate. (b) Calculated strain rate curves (in pct/s) with time from the digitized data.

Table I. Nominal Chemical Compositions (Weight Percent) of the First Generation of FeCrAl Alloys

(Wt Pct)	Fe	Cr	Al	Si	Nb	Zr	C	B
FCA-0Nb	bal.	30.0	3.0	0.2	0.0	0.0	<0.004	<0.001
FCA-1Nb	bal.	30.0	3.0	0.2	1.0	0.0	<0.004	<0.001
FCA-2Nb	bal.	30.0	3.0	0.2	2.0	0.0	<0.004	<0.001
FCA-2Nb-.1Zr	bal.	30.0	3.0	0.2	2.0	0.1	<0.004	<0.001

comparative to alloys produced and tested in this study. The flat dog bone creep specimens were cut from the solution-treated materials using wire EDM. The length of the specimens was approximately 35 mm, by approximately 5 mm across the gauge section and less than 1 mm thick. The creep tests were performed in specially designed direct load creep frames. The entire sample and holder were held at the test temperature in a furnace. The temperature was measured by four-type K thermocouples. The samples were creep tested to failure at 973 K (700 °C) and 70 MPa. The sample length change was measured by an averaging extensometer attached to a plate affixed to the bottom sample holder rod.

C. Microstructure Characterization

For microstructure characterization, the samples were prepared using standard metallographic techniques. A final polish was achieved using 0.05 μm colloidal silica on a Buehler Vibromet II[®] for more than 6 hours. Scanning electron microscopy (SEM) was used for the majority of the characterization. The polished samples were characterized on a JEOL 6500 FEG-SEM at 20 kV equipped with Backscatter, EDAX Electron Backscatter Diffraction (EBSD), and EDAX Energy Dispersive Spectroscopy (EDS) detectors. The matrix composition and Laves phase composition were identified using EDS. EDS was also used to identify undesired phases such as σ - or α -Cr phases if present. Both grain size and Laves phase distribution was measured using the Backscatter detector. The creep fracture surface was imaged on a Hitachi S3400 SEM. The EBSD was used to analyze the misorientation of the Precipitate-Free Zone (PFZ) in the Transmission Electron Microscopy (TEM) thin disks described below.

TEM specimens of the FCA alloys were made using failed creep specimens. The gauge section was sectioned away from the grip using a low speed diamond blade. The sample was polished to less than 100 μm using SiC sandpaper with grits of 600, 800, and 1200. After the samples reached the required thickness, 3 mm round disks were punched out of the gauge section. The disks were then twin jet electro-polished using a solution of 10 pct nitric acid (at a concentration of 100 pct nitric acid) and 90 pct methanol (by volume) at 258 K (−15 °C), 15 volts, and a flow rate of 5 mL/s. The disks were characterized on a ZEISS LIBRA 200 HT FE MC TEM operating at 200 kV. In order to identify dislocations, the samples were imaged along the [100] zone axis under bright field conditions.^[19] Dislocations were identified by their disappearance with slight tilts of the sample off of the [100] zone axis.

Atom Probe Tomography (APT) was used to analyze the composition of the Laves phase on the grain boundaries after solution treatments. Using a dual-beam FEI Nova 200 focused-ion beam (FIB)-SEM, a 12 μm wedge along the grain boundary region was lifted out and transferred onto a Si micro-post array. Before annular milling, the wedge was thinned to approximately 200 nm and the grain boundary was located using the through-the-lens-detector (TLD). Because the direction of the grain boundary through the wedge was

unpredictable and became harder to target as the thickness increased, thinning prior to annular milling was performed to ensure that the grain boundary could be targeted within the center of the APT needle. A series of 30 kV annular milling steps were performed around the grain boundary, such that the grain boundary was contained within the needle. A final low-voltage (2 kV, 75 pA) milling was used to clean the surface from beam damage, ensure the tip apex radius was <100 nm, and to position the grain boundary close to the specimen apex. The Si micro-post array was then inserted into the CAMECA[®] local-electrode atom probe (LEAP 4000XHR) equipped with a 10 picosecond, 355 nm UV laser. The specimen was cooled to a temperature set point of 50 K (−223.15 °C) and then run with a laser energy of 50 pJ, a frequency of 250 kHz, and a detection rate of 0.01 per pulse.^[20] The Integrated Visualization and Analysis Software (IVAS 3.6.12) was used to reconstruct the data.

III. RESULTS

A. Microstructure After Solution Heat Treatment

The initial microstructure, before creep testing, was important to characterize because it affects the creep damage evolution in the FCA alloy system. Ferrite grain size and initial amounts of Laves phase were expected to change the time to failure of the samples. A fully solutionized microstructure was desired to prevent precipitates being present during welding. Figure 2 shows the microstructure of the as-solution heat-treated samples. The 0Nb-containing alloy (FCA-0Nb, see Figures 2(a) and (e)) did not contain Laves phase within the microstructure; an expected result since there were no precipitate-forming alloying additions.

No undesirable σ - or α -Cr phases were detected in any alloys. The FCA-1Nb alloy (see Figures 2(b) and (f)), which has a lower solution temperature (approximately 1273 K (1000 °C)), contained a few small Laves phase particles on the grain boundaries. There were observable amounts of Laves phase present in the matrix of FCA-2Nb and FCA-2Nb-1Zr samples (see Figures 2(c), (g), (d) and (h), respectively). These samples both contained grain boundary Laves phase, large Laves phase particles, and small string-like arrays of Laves phase particles. The large Laves phase particles were also observed after creep testing. It is assumed that the Laves phase remained in the matrix from solidification and did not dissolve during heat treatments. The grain boundaries in these alloys were also decorated with Laves phase. The solutionizing heat treatment for the alloys was chosen based on the information provided by JMatPro[®]. The solutionizing temperature was predicted to be 1413 K (1140 °C). To understand the validity of the JMatPro modeling, the solutionizing temperature was recalculated using the software ThermoCalc[®], using the TCFE7 database. The solutionizing temperature for FCA-2Nb and FCA-2Nb-1Zr in ThermoCalc was found to be approximately 1498 K (1225 °C) (Figure 3). Figure 4 shows the equilibrium weight

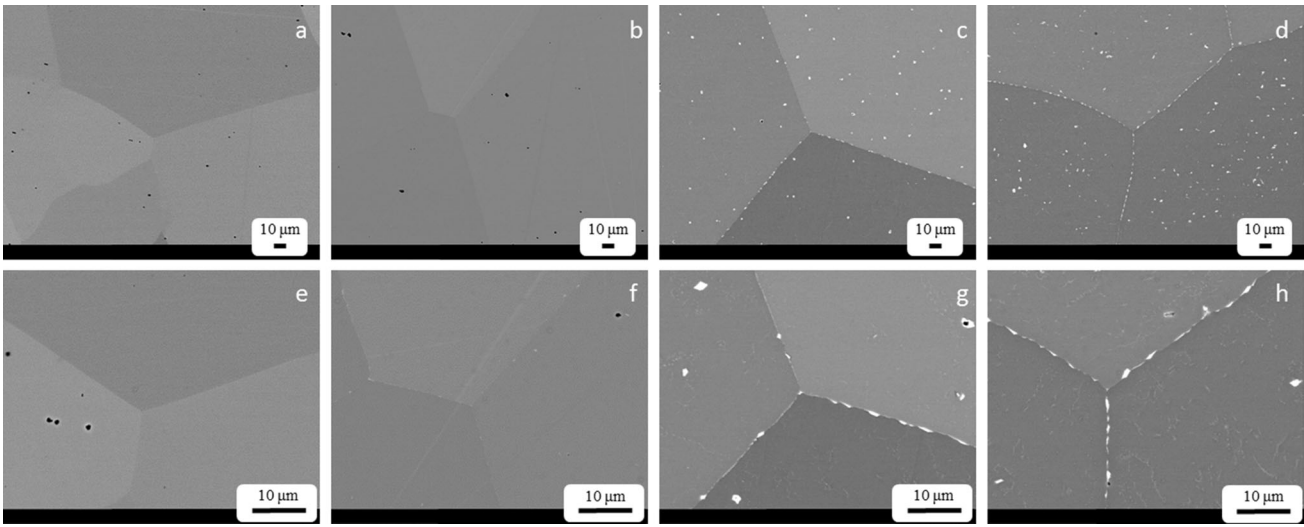


Fig. 2—As-solution heat-treated microstructures. The corresponding alloys are as follows, (a and e) FCA-0Nb, (b and f) FCA-1Nb, (c and g) FCA-2Nb, and (d and h) FCA-2Nb-1Zr. It is observed that 1573 K (1300 °C) for 10 min was not successful in solutionizing the Laves phase.

percent of Laves phase predicted in the alloys as a function of temperature using the two software packages. The two dashed lines are the JMatPro[®] calculated curves. The solid line is calculated from ThermoCalc[®]. The difference shown in the 2Nb lines provided some rationale for the observation that the Laves phase in the 2Nb-containing alloys did not go into solution.

The grain size is considered and is an important variable for creep property comparison. The impact of the grain size on creep mechanisms will be discussed later. Table II shows the grain size in the solution heat-treated samples, measured from images in Figure 2. The standard deviation is large. This means that there is a large variation of the grain size in a single sample. The FCA-2Nb sample in the solutionized condition contained a few grains larger than 600 μm. With the creep samples being small, the grain size could significantly affect results, depending on the local grain size where the specimen was taken from the plate. The grain size differed because of the difference in heat treatment temperatures. The 2Nb-containing alloys were both heat treated at 1573 K (1300 °C) while the other alloys were heat treated at or below 1473 K (1200 °C). The higher heat treatment for the 2Nb-containing alloys created larger grains than the FCA-1Nb sample.

Atom Probe Tomography (APT) was used to understand the Laves phase composition present after the solutionizing heat treatments. Figure 4(a) shows a reconstructed needle from the FCA-2Nb sample with a grain boundary Laves phase intersecting the needle. (The Nb ions highlighted in brown). Figure 4(b) shows only the Nb atoms without the surrounding matrix. A 12 at pct Nb isoconcentration surface was used to define the interface between the Laves phase and the matrix. A proximity histogram of this interface, which is a composition profile with respect to proximity from the interface, is displayed in Figure 4(c); defining the composition profile between the matrix and Laves phase. By

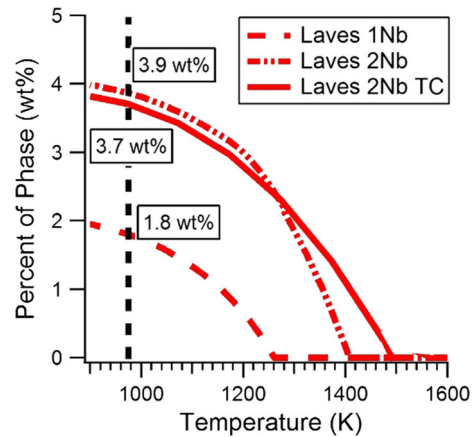


Fig. 3—Calculation of the equilibrium amounts of Laves phase in the Fe-Cr-Al alloy. The figure shows an increase in solutionizing temperature of the FCA-2Nb alloy, which indicates problems with calculating equilibrium of the alloy.

comparing the matrix and Laves phase, it can be seen that the Laves phase is Nb and Si rich, and Fe, Cr, and Al depleted compared to the matrix. It can also be seen that there is an enrichment of Fe and a depletion of Cr at the Laves phase/Matrix interface. The enrichment of Fe is due to the rejection of Fe from the formation and growth of Laves phase. Even though the Fe is a major element in Laves phase, the Fe composition in Laves phase is lower than the Fe composition in the matrix. Therefore, to form Laves phase some extra Fe is rejected into the matrix. The measured depletion of Cr at this region is a consequence of enrichment of Fe. When the density of Fe atoms increases in this region the apparent density of Cr atom will decrease to satisfy a measured percentage of 100 pct. The bulk composition for the matrix was found to be (in atomic percent): 61.8 pct Fe, 31.6 pct Cr, 5.7 pct Al, 0.27 pct Si, and 0.13 pct Nb.

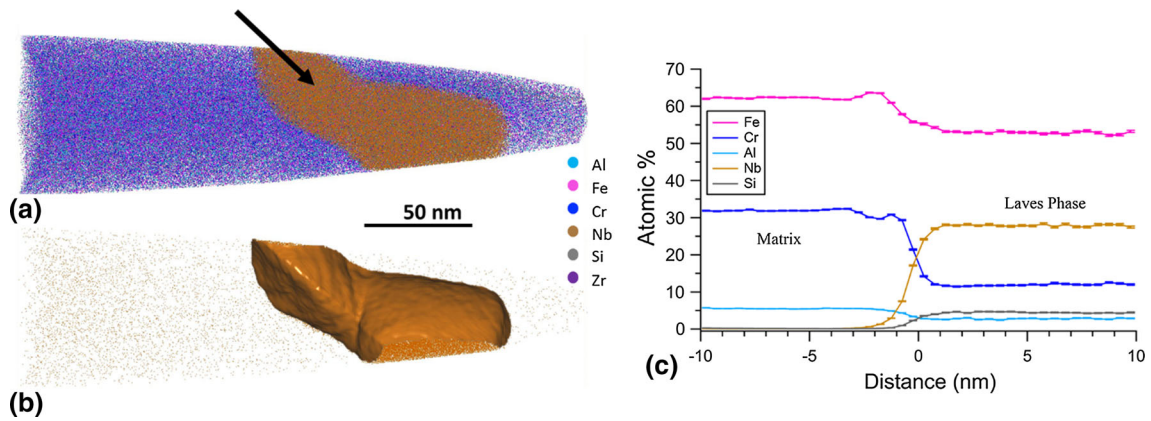


Fig. 4—(a) All ions collected from the FCA-2Nb sample. A grain boundary Laves phase is highlighted with a black arrow. (b) Only Nb atoms are displayed with a 5 at. pct Nb isosurface defining the interface between the Laves phase and the matrix along a grain boundary. (c) Proxigram analysis showing the Atomic concentrations of elements from the matrix to the Laves phase in FCA-2Nb. The laves phase is enriched in Nb and shows stoichiometric equilibrium concentrations.

Table II. BCC Grain Sizes Prior to Creep in Microns

FCA-0Nb	FCA-1Nb	FCA-2Nb	FCA-2Nb-.1Zr
$152.7 \pm 25 \mu\text{m}$	$305 \pm 64 \mu\text{m}$	$467 \pm 188 \mu\text{m}$	$374 \pm 81 \mu\text{m}$

The bulk composition for the Laves phase was found to be (in atomic percent): 53.5 pct Fe, 26.9 pct Cr, 2.85 pct Al, 4.5 pct Si, and 26.9 pct Nb. The comparison between the bulk compositions of the matrix and Laves phase shows that most of the Nb partitioned to the Laves phase. In addition, the Laves phase composition calculated from the APT experiment was close to equilibrium conditions, which was predicted using ThermoCalc[®], (matrix: 62.9 pct Fe, 30.4 pct Cr, 6.1 pct Al, 0.29 pct Si, and 0.14 pct Nb and Laves phase: 52.8 pct Fe, 28.3 pct Cr, 1.4 pct Al, 3.5 pct Si, and 24.4 pct Nb in at pct). The implications of these findings are that simple coarsening models can be used to model the evolution of the grain boundary Laves precipitate size distribution. This information can then be used to optimize the alloy for better creep resistance.

The alloy containing Zr had almost 100 μm smaller grain sizes. It is reported that Zr is a common grain refiner in aluminum alloys.^[21–23] Similar mechanisms are possible for the FCA system. APT measurements revealed Zr partitioning to the Laves phase, which was confined to the grain boundaries. Figure 5(c) shows the partitioning of Zr in the Laves phase confined to the grain boundaries for FCA-2Nb-.1Zr alloy, in which there was only 0.02 at pct Zr in the matrix. Possible mechanisms for the grain size reduction with the addition of Zr are hypothesized as follows: Zr segregates to the ferrite grain boundaries during solidification or during heat treatment. The Fe-Zr phase diagram shows almost no solubility for Zr in Fe-BCC even at 1573 K (1300 °C).^[24] According to the Fe-Nb phase diagram, Nb is soluble (approximately 3 wt pct) in Fe-BCC at 1573 K (1300 °C).^[25] Therefore, during heat treatments the grain growth could be slowed, before the

precipitation of the Fe₂Nb Laves phase with preferential enrichment of Zr. The high concentration of Zr at the grain boundary could have driven the local equilibrium thermodynamics to nucleate Fe₂Zr Laves phase. During subsequent slow cooling and low temperature heat treatment, Nb could have diffused into the Zr-rich Laves phase to form the equilibrium Laves phase with both Nb and Zr, *i.e.*, Fe₂(Zr, Nb), as well as, independent Fe₂Nb Laves phase. Although the above microstructure evolution is not proven, the presence of α/α grain boundary precipitates might have slowed the grain growth in FCA-2Nb sample.

B. Microstructure After Aging

In the present research, two alloys (FCA-1Nb & FCA-2Nb) were chosen for aging studies. The microstructures after aging for 168 hours at three different temperatures 973 K, 1073 K, and 1173 K (700 °C, 800 °C, and 900 °C) are shown in Figure 6. The size and density of the Laves phase can be measured from these images. For ease of calculation, the number density and size measurements did not consider the Laves phase on the grain boundary. Images from the center of a few grains were chosen at random for measurements. The results demonstrate that as the aging temperature increased, the coarsening rate also increased with a concurrent increase in the size of Laves phase and decrease in the number density. The sizes remain similar between the FCA-1Nb and FCA-2Nb samples for each of the three temperatures. The coarsening rate (approximately 5×10^{-26} m/s) of Laves phase is similar in both alloys and is not influenced by additional Nb. However, the number density is larger

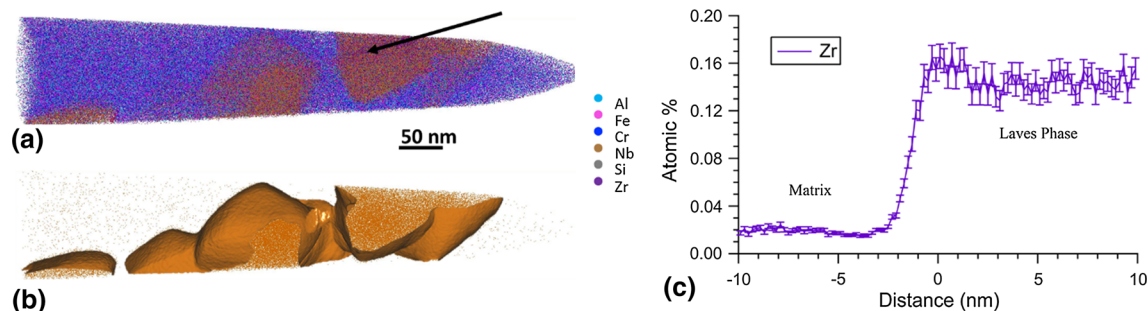


Fig. 5—(a) All ions collected from the FCA-2Nb-1Zr sample. A grain boundary Laves phase is highlighted with a black arrow. (b) Only Nb atoms are displayed with a 5 at. pct Nb isosurface defining the interface between the Laves phase and the matrix along a grain boundary. (c) Atomic concentrations of Zr from the matrix to the Laves phase. Zr is seen to enrich in the Laves phase along the grain boundary. Note that the magnitudes of the other elements' atomic concentrations for FCA-2Nb-1Zr are the same as Fig. 4(c).

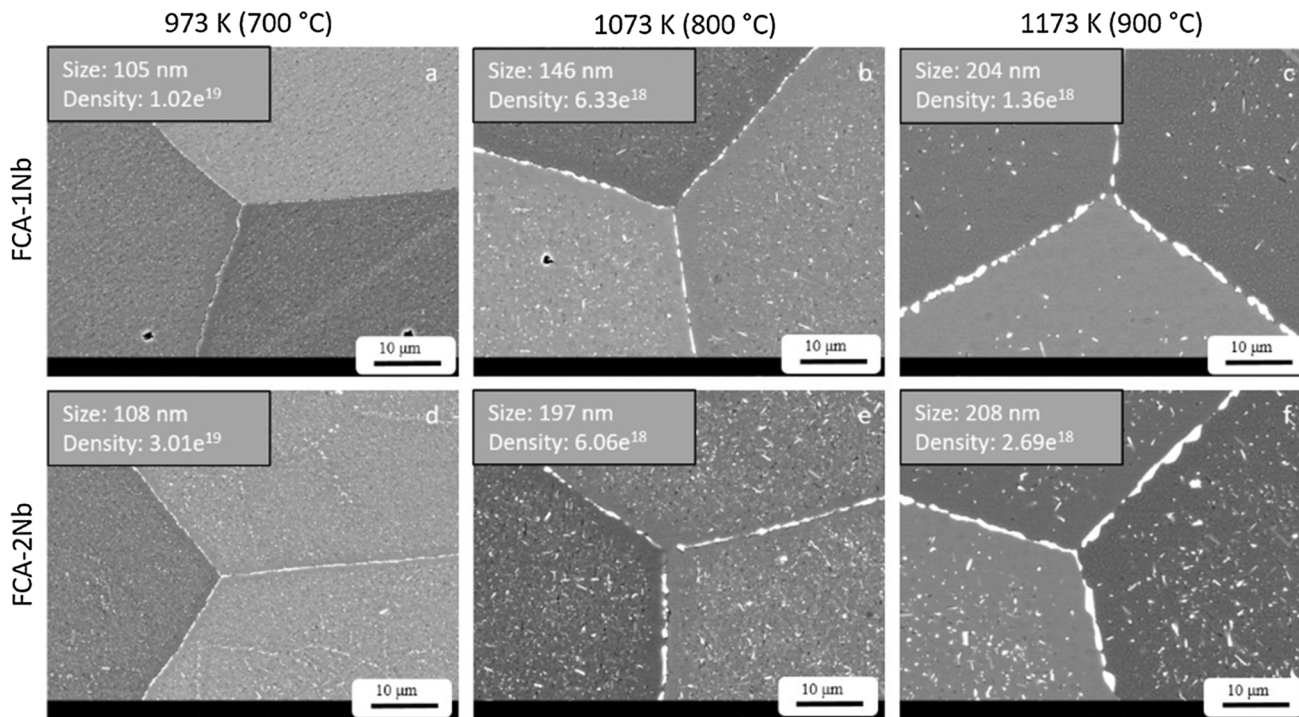


Fig. 6—Microstructures from aging 168 h at three different temperatures.

in the FCA-2Nb sample, which can be explained by the alloy containing more Nb. The same trend can also be seen after aging for 1008 hours. This is shown in Figure 7. The size of Laves phase between the two alloys was similar at each temperature, where the sizes were found to be approximately 100 nm, (150 to 200) nm, and 200 nm for 973 K, 1073 K, and 1173 K (700 °C, 800 °C, and 900 °C), respectively. However, the Laves phase number density of the FCA-2Nb alloy remains slightly larger, but is within the same order of magnitude. At 973 K (700 °C) the size of the Laves phase in both alloys coarsens by approximately (20 to 30) nm, while the number density remains fairly stable. The result shows that the Laves phase in the FCA alloy system has a low coarsening rate at 973 K (700 °C) up to 1000 hours. The aging studies indicate that Laves phase is a good candidate for the creep resistance in the FCA alloy system.

Along with the fraction of Laves phase, the PFZ is also an important aspect in the FCA alloys. Initially the PFZ forms by the precipitation of grain boundary Laves phase, and depleting all the Nb from the surrounding matrix.^[26,27] With further aging, the PFZ increased in size because of continued growth of Laves phase at the grain boundaries. (The size of the PFZ is the average distance from the grain boundary to the beginning of the matrix Laves phase on one side of the grain boundary.) The sizes of the PFZ for FCA-1Nb and FCA-2Nb samples at 973 K (700 °C) and 168 hours were measured at 0.93 and 0.84 μm, respectively. After aging to 1008 hours, the size of the PFZ for FCA-1Nb and FCA-2Nb was found to be 1.13 and 1.04 μm, respectively. The reduced size of the PFZ in the FCA-2Nb sample is attributed to higher Nb in the matrix, and thus more Laves phase present closer to the grain boundary for the same time.

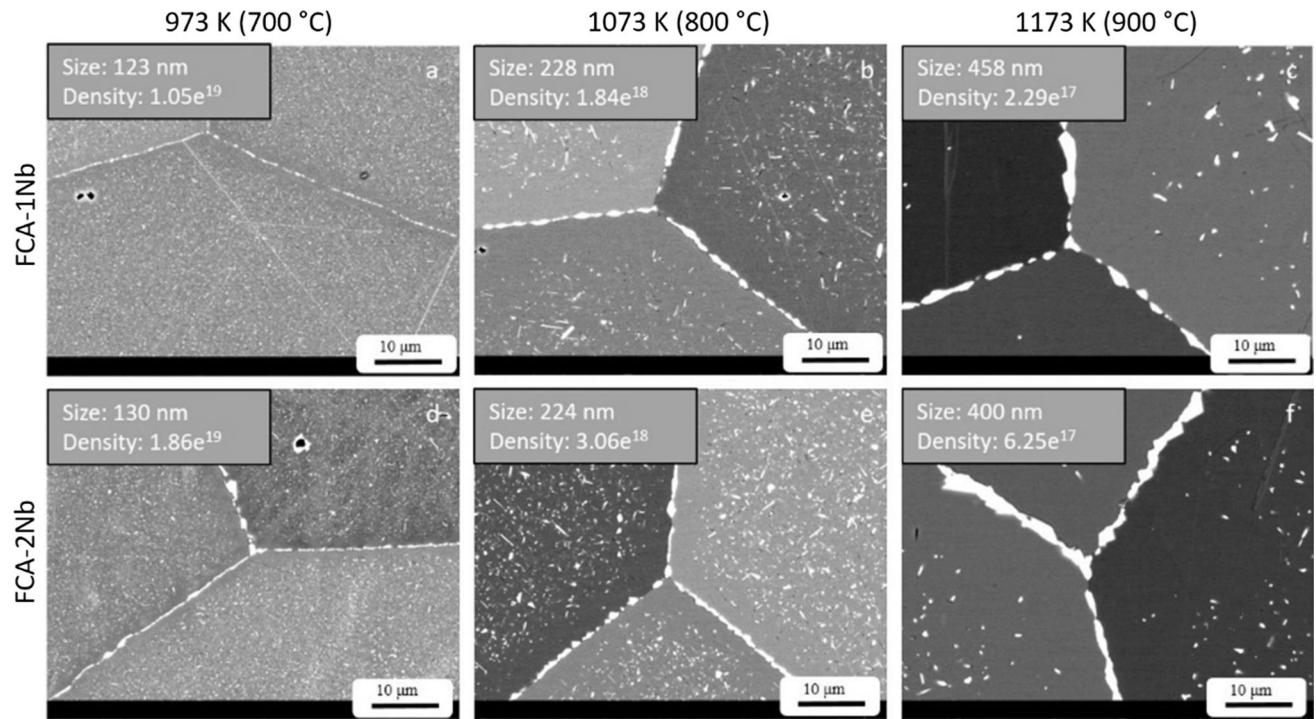


Fig. 7—Microstructures from aging 1008 h at three different temperatures.

C. Post Creep Test Microstructure and Fractography

1. Fractography

The SEM images (see Figure 8) suggest a mechanism of ductile failure at the grain boundary. In Figure 8(a), the grain boundary failure and shear from final fracture can be observed in FCA-2Nb. An explanation is proposed. The grain boundary, on the left of the image labeled grain boundary failure, could have accumulated creep voids during testing. With further testing time, the grain boundary separated along these voids and the ductile PFZ region. With continued separation of grain boundaries, the load partitioning occurred with the matrix region due to the 3D geometry of the grains. This lead to an increase in effective stress, and creep rate accelerated. At a critical reduction of load bearing area, the sample pulled apart, creating the ductile shear fracture. The explanation is supported by other fractography images indicating grain boundary failure with Laves phase in ductile cups (see Figure 8(b)). The presence of Laves phase being within the ductile cups confirmed the cavity formations around the Laves phase. Even in the flat grain boundary failure region, ductile cups with Laves phase inside was observed. Irrespective of minor differences in microstructures (see Figures 6 and 7), the fractography showed similar failure morphologies between the two alloys. Figure 8(c) is the fractography of the FCA-1Nb sample. Here, the distinctive grain boundary ductile failure can also be observed.

2. SEM imaging

The microstructures (obtained *via* backscatter imaging) of the three Nb-containing alloys after creep failure

are shown in Figure 9. Figures 9(a) to (c) shows the top face of the creep failure tip (normal to the surface). The FCA-1Nb and FCA-2Nb samples had observable ductility at the fracture tip. From the images, it appears that these two samples failed *via* a grain boundary failure mechanism, but were held together with a few large grains. This can be observed in the FCA-2Nb sample. Figure 9(b) shows a recessed region of the sample at the bottom of the micrograph. Here the grain boundary failed, leaving the large grain at the top of the image to carry the load for the remainder of the creep test. Voids accumulated on the grain boundary in both the FCA-1Nb and FCA-2Nb. Creep voids were observed both near large Laves phase, along the grain boundaries, and on triple points. This indicates a possible grain boundary interaction leading to failure. More voids can be observed in the FCA-2Nb sample because it had a longer time for creep to occur and thus accumulated more voids.

The Zr-containing alloy (FCA-2Nb-1Zr) showed little ductility at the tip. From a sample in the as-solutionized condition, internal grain boundary cracking was observed and may have also been present in the creep specimen before testing. The gauge section contained full grain boundary separation after the creep test (see Figure 9(f)). These observations are likely due to a weakening of the interface between the Laves phase and the matrix with the addition of Zr. From atom probe tomography, Zr was found in the Laves phase along the grain boundaries in the as-received samples and would be expected to remain during creep. As discussed earlier, it is unclear the mechanisms that Zr plays in the strength of the grain boundary. With the

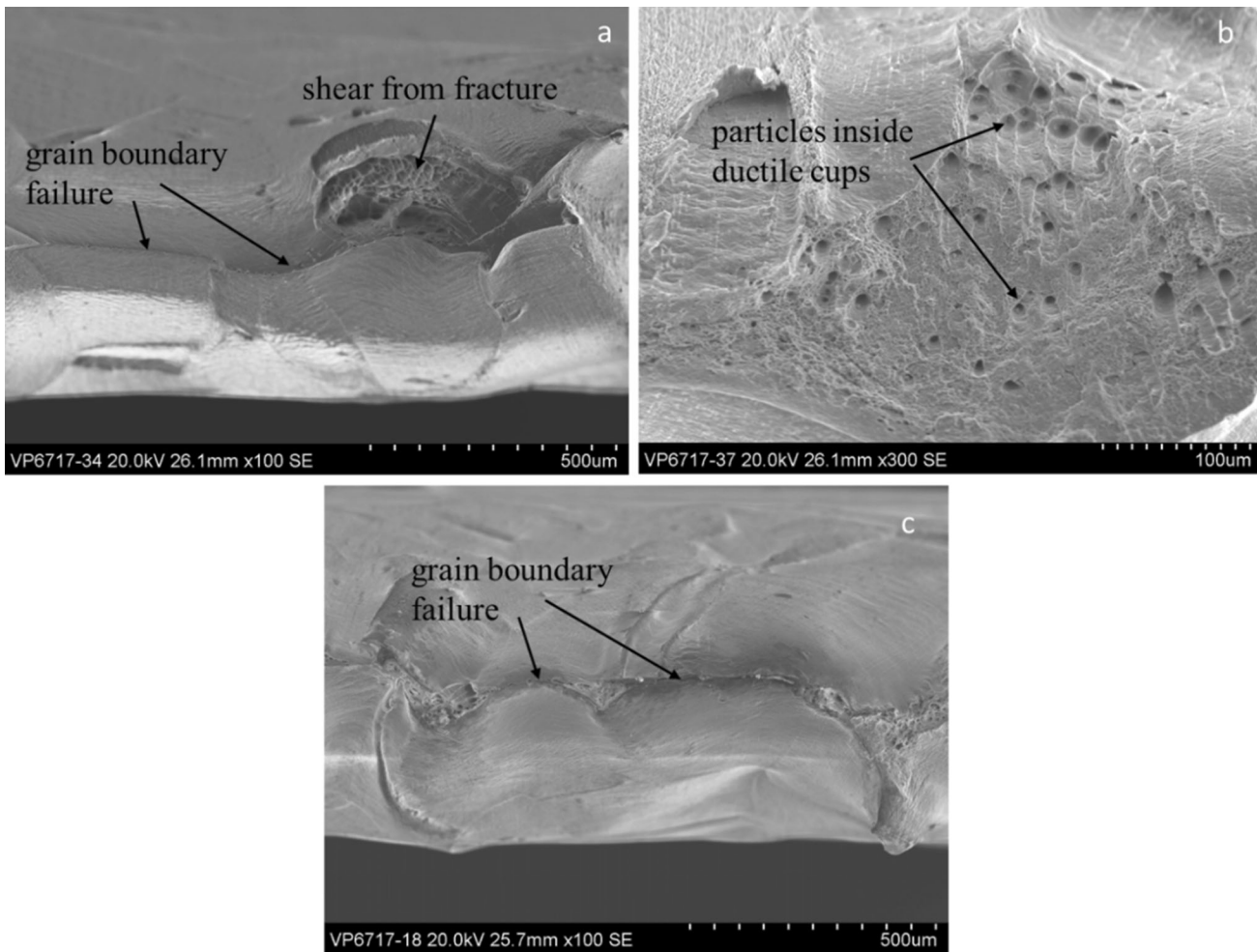


Fig. 8—Selected fractography from creep rupture samples FCA-2Nb (*a* and *b*) and FCA-1Nb (*c*). (*a*) Macrograph showing grain boundary failure and some local shear from final fracture. (*b*) A magnified image of (*a*), Laves phase can be observed inside the ductile cups. (*c*) Grain boundary failure in sample FCA-1Nb.

observed abrupt failure, and the microstructural features, it can be assumed that this sample failed *via* a brittle grain boundary fracture, compared to ductile failure in other samples.

The gauge section in all the samples revealed little creep deformation when observed with the backscatter detector, *i.e.*, there was no evidence for subgrain formation along the grain boundaries. The grains were still large with unobservable elongation and the strain contrast was limited. The matrix particle size and distribution in the FCA-1Nb alloy appeared similar to the aged condition. Although the matrix conditions in FCA-2Nb were similar to aged conditions (1008 hours aging condition), grain boundary voids were observed. There were also voids around the excessively large Laves phase particles within the grain interior. The excessively large Laves phase was shown to be present in the matrix prior to creep. The voids along the grain boundaries may likely indicate Grain Boundary Sliding (GBS), but the PFZ along the grain boundaries requires further investigation. Since the PFZ does not contain Laves phase, dislocations may be able to easily move just as in an alloy with no precipitates.

Figures 9(g) through (i), show the grain boundary region within the gauge section (without voids). The size of the Laves phase in the matrix of the FCA-2Nb alloy (138 nm) is significantly larger than the size (95 nm) of the Laves phase in the FCA-1Nb alloy. However, the FCA-2Nb alloy was held at temperature for a longer period of time, which would have led to coarsening of Laves phase. The number density of Laves phase in the matrix were also similar to each other. The number density for the FCA-2Nb alloy was found to be 1.15×10^{19} and 1.88×10^{19} for the FCA-1Nb alloy. The reason for the lower number density in FCA-2Nb can also be attributed to coarsening. A more significant difference in the alloys is seen in the area fraction of Laves phase along the grain boundaries. The area fraction of Laves phase on the grain boundaries, in the gauge section of the FCA-2Nb alloy is 0.79, while the 1Nb-containing alloy has an area fraction of 0.48. A PFZ along the grain boundaries can be observed in all the alloys. The FCA-1Nb alloy has a PFZ that is (0.8 to 0.9) μm . While the FCA-2Nb alloy has a PFZ that is (1.4 to 1.5) μm . The significance of this difference will be discussed in the discussion section as it pertains to the creep mechanism and failure.

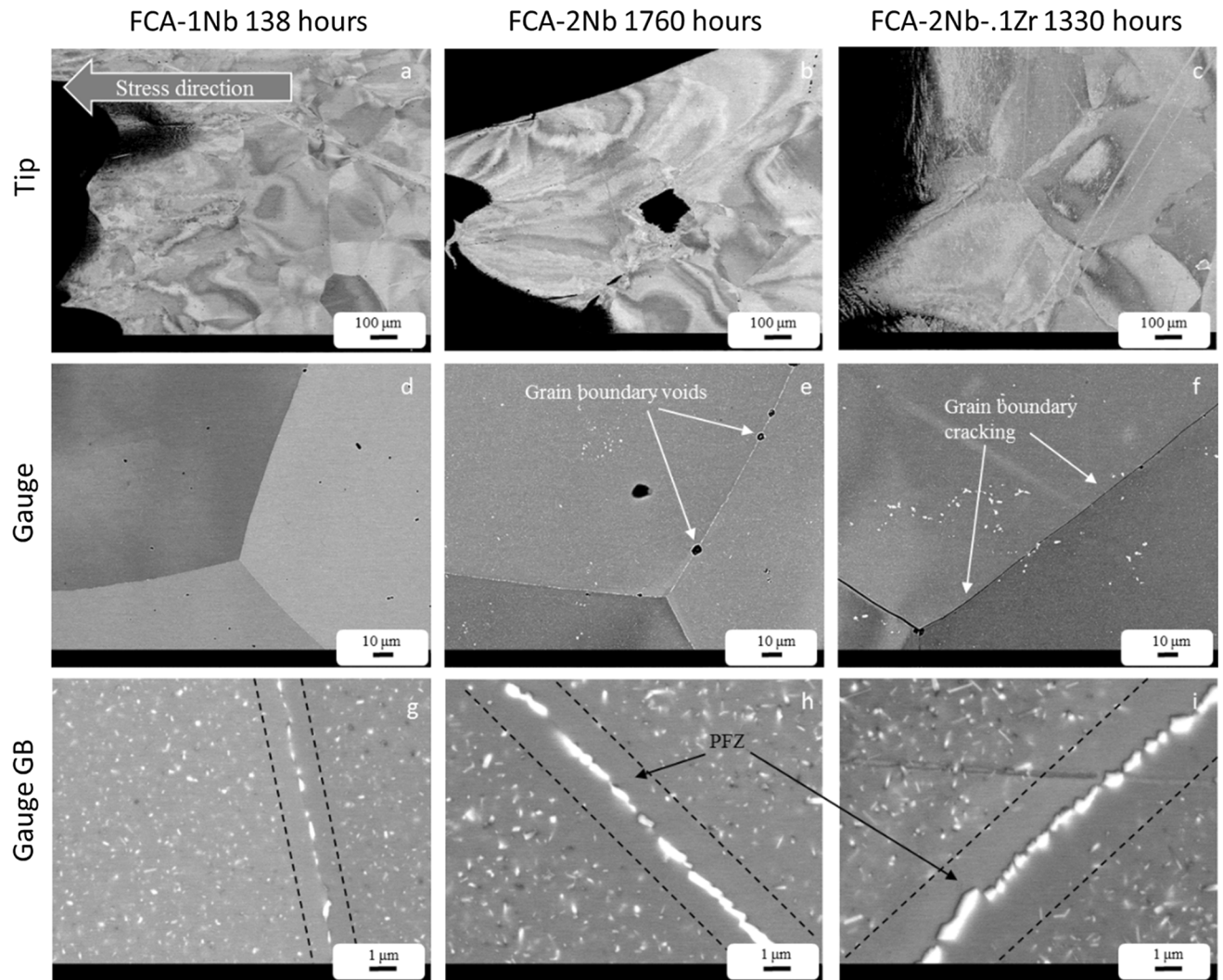


Fig. 9—SEM micrographs of the creep specimens from the top surface. (a to c) fracture tip, (d to f) low magnification of the gauge section, and (g to i) higher magnification of the gauge section at a grain boundary.

3. TEM characterization

Selected TEM images from the FCA alloys are illustrated in Figure 10. An example of the Laves phase in the grain interior can be seen in Figure 10(a). All the samples appeared to have very similar number densities and sizes of Laves phase and were almost indistinguishable between the alloys. This confirms the quantitative analysis performed with the SEM. A low interparticle spacing can be observed within the TEM images, which may aid in pinning dislocations. Multiple morphologies of the Laves phase (*i.e.*, rounder-marked by yellow arrow and lenticular-marked by red arrow) were also observed (see Figure 10(a)). The multiple morphologies observed are most likely due to a sectioning effect. The rod or lenticular Laves phase is randomly aligned with the observed direction; with sectioning, multiple morphologies are observed depending on the intersection geometry of the cut with the Laves phase. In Figure 10(b), a dislocation is pinned by a Laves phase particle. It is known that a dispersion of particles can pin dislocations and an extra shear stress is then required to bow the dislocation through an array of

particles.^[28–30] Figure 10(a), reveals a large array of particles with a small interparticle spacing between (100 and 140) nm. This array of particles can effectively pin dislocations. The grain boundary region differs from the grain interior. Figure 10(c) shows the PFZ next to the grain boundary. The image reveals large Laves phase on the grain boundary, a region without Laves phase, then a transition region where Laves phase particles begin to appear in the grain interior. Because there are no Laves phase particles in the PFZ, the dislocations could freely move and form subgrain boundaries or pile up along the grain boundary. Dislocations are observed piling up on the grain boundary Laves phase in Figure 10(c), and the pile up ends at a small precipitate-free region of the grain boundary.

IV. DISCUSSION

A. Strain Rate Prediction

The creep mechanisms are related to the initial microstructure and the evolution of the microstructure

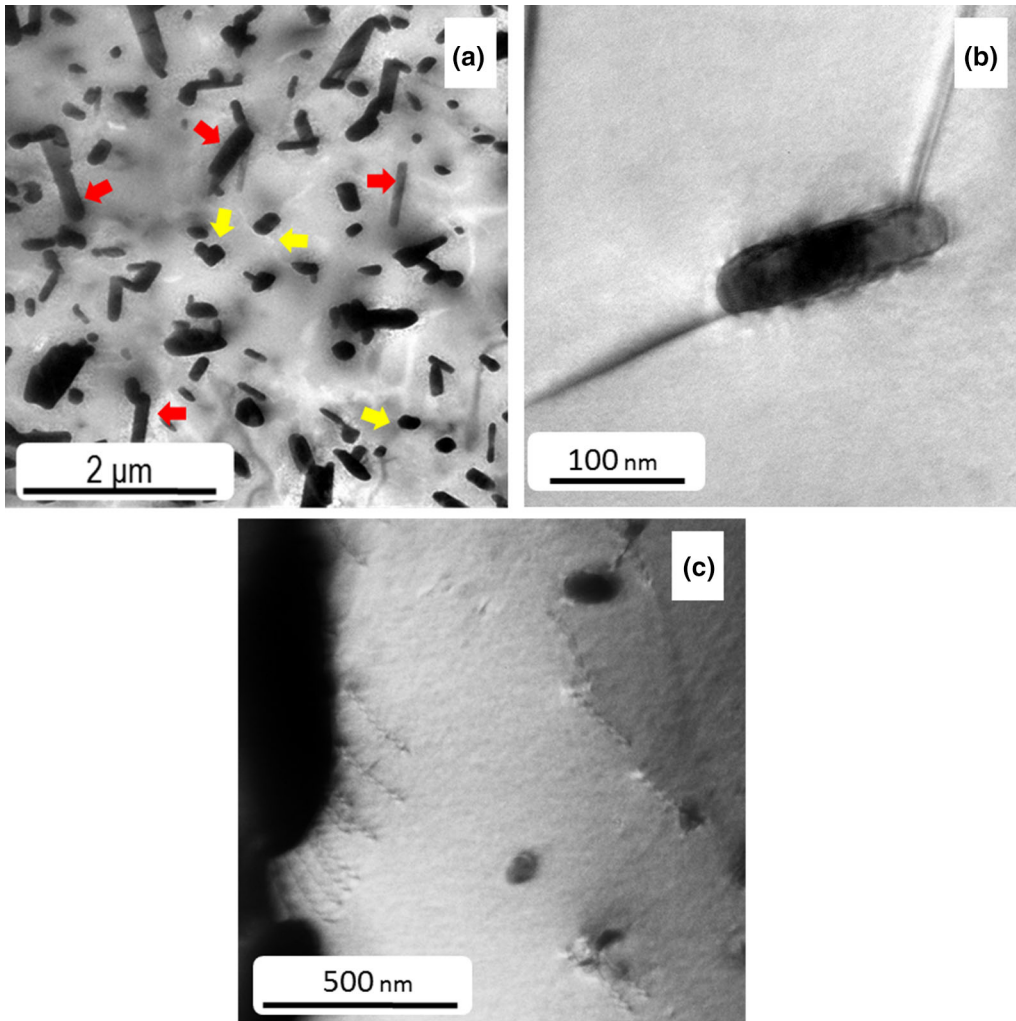


Fig. 10—(a) TEM micrograph of Laves phase imaged in grain interior, strain contrast can be seen as the white lines, from sample FCA-2Nb. (b) Example of dislocation being pinned by a matrix Laves phase particle in the grain interior, from sample FCA-2Nb. (c) Dislocations imaged on the [100] zone axis seen piling up on a grain boundary Laves phase, indicating deformation in the PFZ, from sample FCA-1Nb.

during testing or service. It is difficult to model the evolution of the microstructure with respect to the macro- and micro-level strains within a sample as a function of time. However, researchers have derived equations that could be used to model the performance of a metal under creep by calculating the steady-state or minimum creep rate. The Bird–Mukherjee–Dorn (BMD) equation is a phenomenological equation that relates several parameters to predict the minimum creep rate.^[31]

$$\dot{\epsilon}_{\min} = AD_0 \exp\left(\frac{-Q}{RT}\right) \frac{Gb}{kT} \left(\frac{b}{d}\right)^p \left(\frac{\sigma}{G}\right)^n, \quad [1]$$

where A is constant, D_0 is diffusivity, Q is the diffusion activation energy, R is the gas constant, T is temperature. G is the shear modulus, b is the burgers vector, k is Boltzmann's constant, d is the grain size, and σ is the applied stress. The p and n are the grain size and stress exponent parameters. These exponent parameters are derived from extensive data analysis conducted over

several decades, to find the correlation between these parameters and different creep mechanisms in metals and alloys. The equation relates diffusion (or temperature), the shear modulus of the material, and stress to predict the minimum strain rate. Because these exponent parameters are independent and can cover a large range, researchers have modified these equations to construct creep mechanism maps.^[32,33] These maps break up the wide range of stresses and temperatures based on mechanisms. With further examination of the equations, other important factors may also play a role in determining the minimum strain rate. The grain size can change the creep rate drastically, and may even exceed rates from dislocation mechanisms under certain cases. Since the grain size control can be achieved through heat treatments or thermo-mechanical treatments, researchers have also constructed deformation maps as a function of grain size.^[34] Although these maps constructed for pure metals or solid solution alloys are useful, the maps neither directly correlate to the

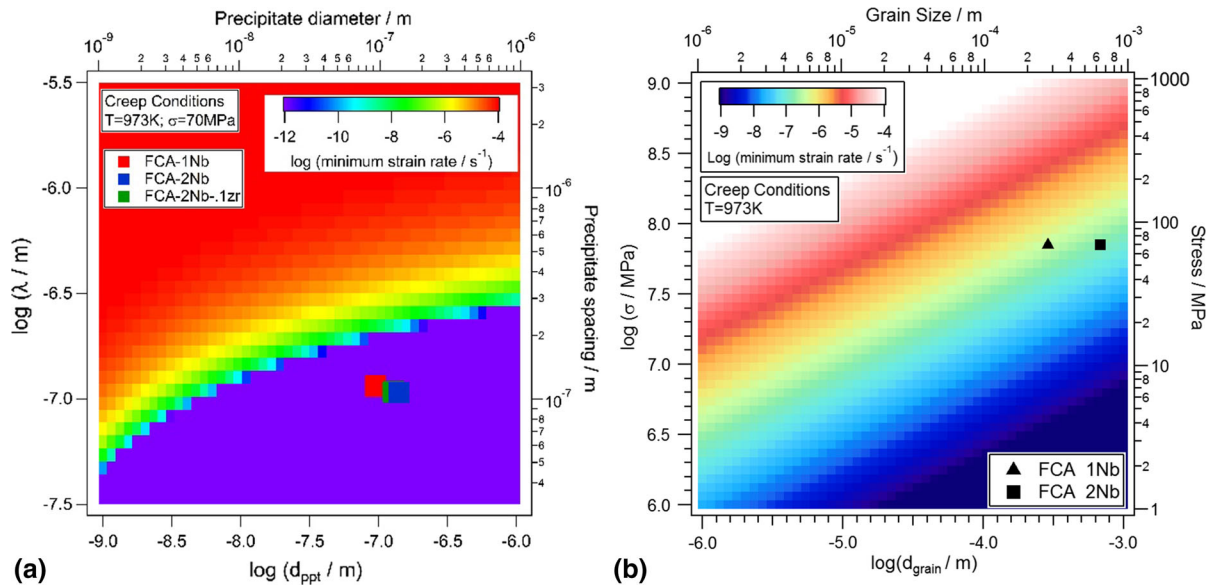


Fig. 11—(a) Recalculation of the strain rate calculated map under the creep conditions for the FCA alloys. Overlaid are the numerical results of the Laves phase from the gauge section after creep failure. (b) Calculations of minimum creep rate (in pct s⁻¹) using BMD phenomenological model as a function of grain size and stress.

multi-component precipitate-strengthened structural steels and alloys, nor describe relative contributions of different creep mechanisms. However, modifications to the BMD equation could provide a pathway to relate the microstructure of a particular structural steel or alloy to a creep mechanism.

B. Evaluation of Creep Mechanism Model in Fe-Cr-Al Alloy

In previous work, the BMD equation was used to predict the minimum strain rate based on particle size and distribution with reference to Grade 91 steel using a threshold stress.^[35] For Grade 91, it was revealed that the carbides would coarsen during welding, and the increase in strain rate could be tracked on a calculated strain rate map. Figure 11(a) is a calculation of the strain rate map under the creep test conditions used for the FCA alloys [973 K (700 °C), 70 MPa] utilizing the threshold stress. The experimental results of interparticle spacing and particle size of Laves phase, measured from the gauge section of the failed creep samples, were overlaid on the map. The points on the map showed that the size and interparticle spacing are not drastically different from each and would suggest that these alloys would have similar creep strain rates. These points lie outside the region for dislocation creep, *i.e.*, the dislocations should be pinned by the Laves phase. Furthermore, calculations showed that the threshold stress is larger than the applied stress. The strain rates predicted from the BMD dislocation model suggest that the strain rates should be on the order of 10⁻¹² s⁻¹. However, the measured steady-state strain rates for the alloys are as follows: FCA-1Nb, 1.75 × 10⁻⁶ pct s⁻¹, FCA-2Nb, 1.47 × 10⁻⁷ pct s⁻¹, and FCA-2Nb-1Zr, 9.23 × 10⁻⁸ pct s⁻¹. The results suggest that another creep mechanism is likely operating.

Based on literature results, the creep conditions in this study and the large grain size in the samples, we postulate that the GBS mechanism may be the likely creep mechanism.^[36] Langdon,^[37] has recently shown deformation maps to include GBS. The BMD equation can now be reanalyzed to correlate the microstructure of the FCA alloys to creep rate. The following is the BMD equation used for modeling of GBS in the FCA alloys.^[38]

$$\dot{\epsilon}_{min} = A_{GBS} D_0 \exp\left(\frac{-Q}{RT}\right) \frac{Gb}{kT} \left(\frac{b}{d}\right)^1 \left(\frac{\sigma}{G}\right)^2 \quad [2]$$

Here, A_{GBS} is the GBS constant and was taken as 10 for the model.^[37] The p exponent here is 1 and the stress exponent is 2.^[37] Figure 11(b) is a calculation of the BMD model using Eq. [2]. The strain rate map suggests that the smaller the grain size the faster the creep rates. This is because of the increased amount of grain boundaries allowing more deformation to occur in a given time. Overlaid on the map are the points representing the grain size from the FCA-1Nb and FC-2Nb samples. The calculated strain rate for the FCA-2Nb sample is 1.57 × 10⁻⁷ pct s⁻¹ which is similar with the observed strain rate of 1.47 × 10⁻⁷ pct s⁻¹. The new model considering the GBS does correlate with observed strain rates.

It is necessary to use the observed microstructural evidence to understand the creep mechanism in the current alloys. The dislocation model for the interior of the grain clearly shows that dislocations are pinned and a grain boundary mechanism is operating. The microstructures clearly show grain boundary Laves phase and a PFZ. How these complex microstructural distributions play into the competition between creep in the grain interior and the boundaries prompted, further characterization within the PFZ regions.

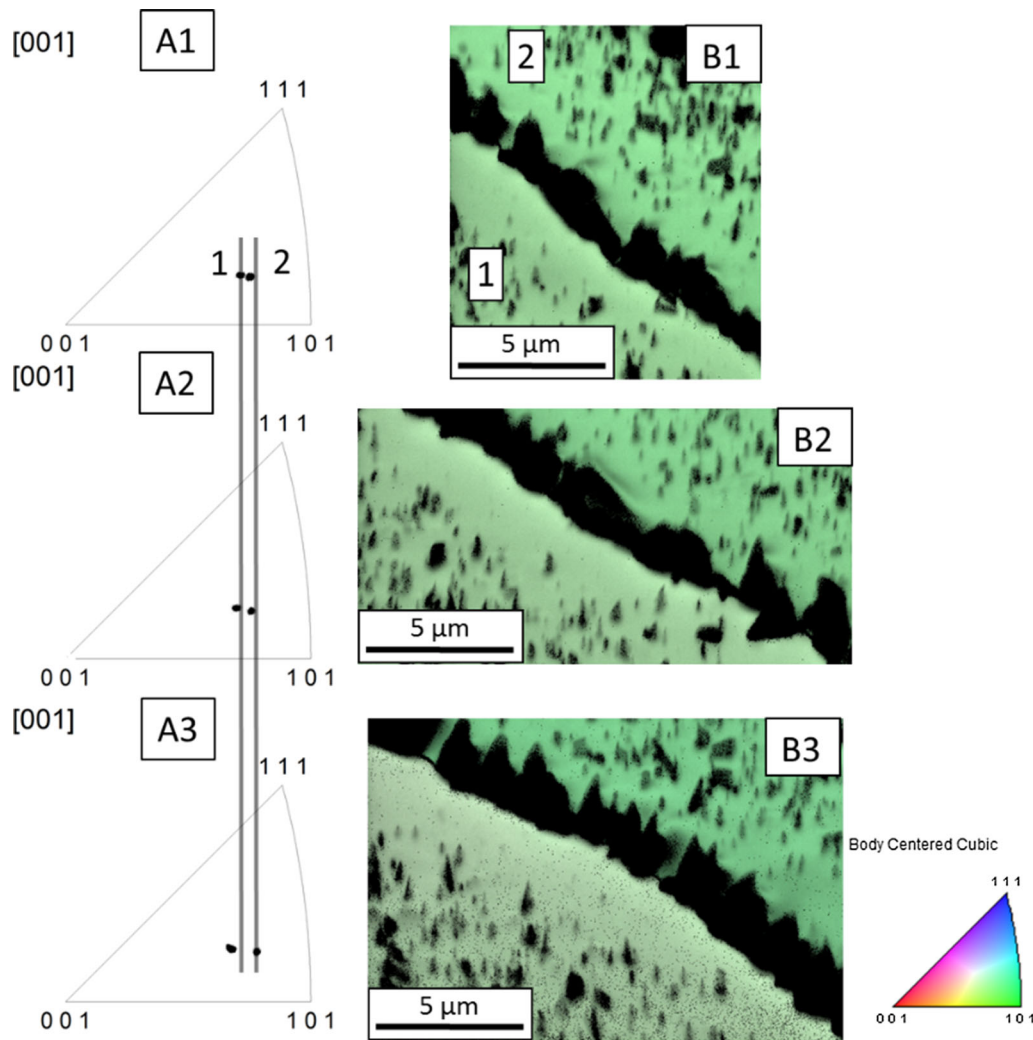


Fig. 12—(A1 through A3) Inverse pole figures from the EBSD mapping showing the orientation of grains 1 and 2. The orientation change can be observed from the pole point shifting from the straight vertical line. (B1 through B3) EBSD maps of a grain boundary region in the FCA-2Nb creep-ruptured sample. The low confidence indexed pixel of Laves phase has been extracted.

C. Creep Deformation in the Precipitate-Free Zone of Fe-Cr-Al Alloys

Due to a lack of Laves phase in the PFZ region, it was assumed that the PFZ deformed preferentially instead of the matrix. The PFZ should therefore have a faster creep rate than the matrix. However, the validity of the hypothesis requires proof of plastic deformation in the PFZ of the creep-ruptured sample.

Using EBSD, the crystallographic orientation of the grains was mapped and measured. Figure 12 shows the inverse pole figure [(A1) through (A3)] and EBSD patterns [(B1) through (B3)] from three regions along a grain boundary in the gauge section. The black regions in the EBSD patterns are low confidence index pixels associated with the Laves phase and were partitioned out from subsequent analyses. From Figure 12(A1) through (A3), the orientation of grain 1 changes as a function of the location. The point on the inverse pole figure is observed to diverge from the superimposed vertical line, which is an indication of rotation within grain-1 with respect to grain-2. This observation of

crystal rotation is considered indirect evidence for deformation in the PFZ. The above mechanisms can be visualized in terms of a “core and mantle” model.^[39] The center of a grain has a large density of Laves phase particles and low interparticle spacing. Under those conditions, the motion of dislocations is stifled by interaction with Laves phase, thus creating a strong immobile core. The PFZ, which does not contain Laves phase, can be viewed as the “mantle,” which allows the movement of dislocations freely. Continual movements of the dislocations and rearrangement of the dislocation into subgrain structures in the PFZ allow for the observed global rotation of the grains.

The arrangements of dislocations into subgrain boundaries can be globally observed with small <1 deg misorientation changes. Figure 13 represents two point to origin line profiles from the matrix and the PFZ. The line profile for the matrix shows little change over the distance of the measurement. This is indicative of the “core” model where the grain interior did not rotate within itself. On the other hand, the line profile within

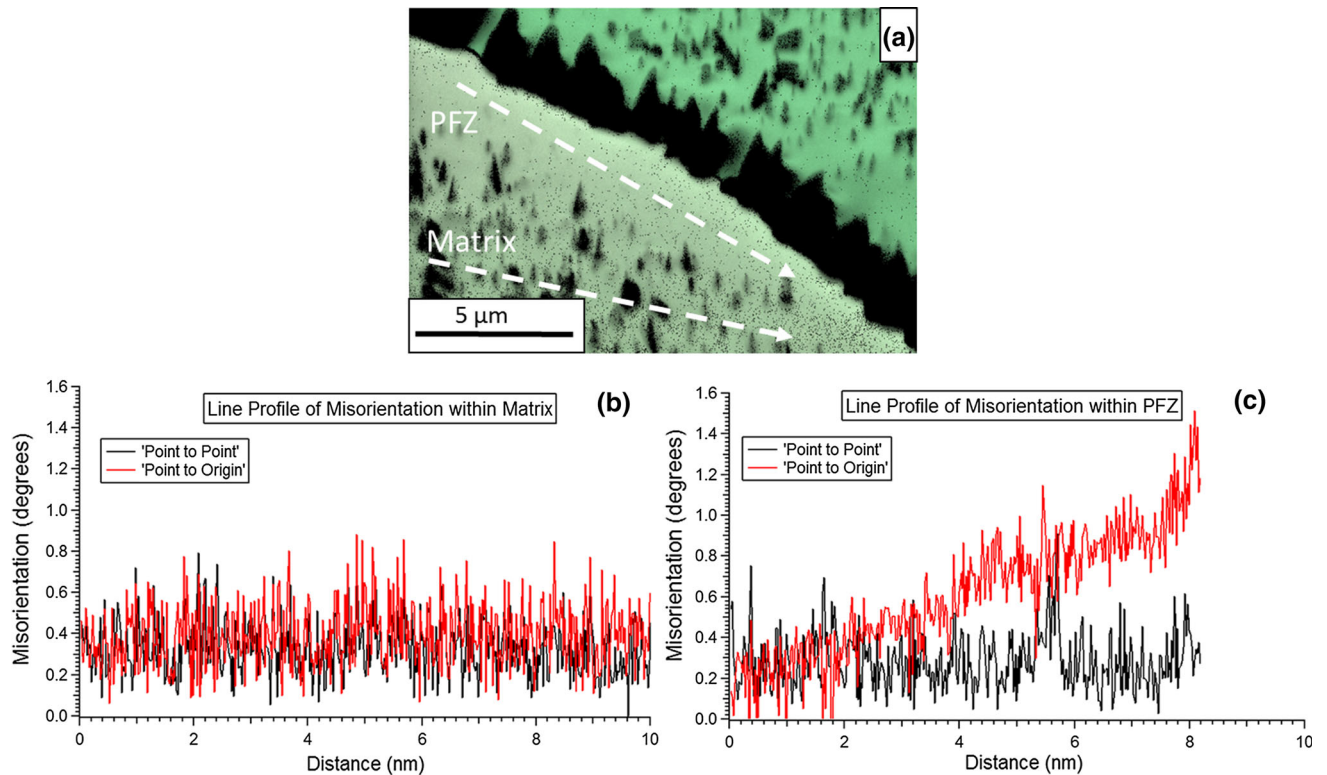


Fig. 13—(a) Selected grain boundary region, representative arrows show different locations of line profiles. (b) Line profile measurement of the matrix, the graph shows little misorientation change from the origin. (c) Line profile measurement of the PFZ, the graph indicates misorientation changes along the PFZ.

the PFZ does show orientation changes in the point to origin profile. This indicates that the PFZ contained the deformation by dislocation movement and subgrain formation. With continual subgrain formation and growth along with added dislocations, voids could nucleate at the intersection of the subgrain boundaries and the grain boundary. As the ratio of the fraction of Laves phase on the grain boundary and the width of the PFZ drops below certain conditions then the condition is favorable for failure. The “core and mantle” model illustrates the complex competition of multiple creep properties within the alloy, which can also make it difficult to describe the global creep properties of selected alloys.

Although, the above hypothesis and evidence for the grain orientation and subgrain formation in the PFZ appears to be valid, we believe that the above measurements do not consider the inherent error in the EBSD measurement techniques. Therefore, future research must leverage other high-resolution characterization tools that are based on fine-scale probes, such as advanced photon sources.

D. Correlation of Grain Boundary Characteristics to Creep Rupture Properties

Table III gives a comparison of the area fraction of Laves phase on the grain boundary and the width of the PFZ. First, it is reasonable to assume that the smaller the area fraction of Laves phase, it would lead to higher

amount of creep cavity nucleation on the free grain boundary areas, or grain boundary regions that are devoid of precipitates. It could be seen that there is some area fraction of Laves that evolves during creep that would allow more cavity nucleation, eventually linkage, and failure. The FCA-1Nb sample does have a low area fraction of Laves phase and failed quickly. However, the FCA-2Nb sample maintained a large area fraction of Laves phase on the grain boundary even with failure. On the other hand, there may be a width of the PFZ that allows more deformation adjacent to the grain boundary. With the lack of precipitates, the dislocations are free to move, allowing for faster rates of deformation in the PFZ. The results suggest a contradiction to the results of precipitate areal fraction on the grain boundary. The FCA-1Nb failed with a smaller width of the PFZ while the FCA-2Nb lasted longer with a larger PFZ. The measurements of PFZ were performed normal to the creep specimen and in the transverse direction. This was done to eliminate the possibility of geometric effects from orientation of the grains to each other. The width of the PFZ does not support the hypothesis that only one parameter can be used to understand the failure. The PFZ should always be deforming after it reaches some minimum width. The matrix within the PFZ is similar to the matrix of the FCA-0Nb sample. Therefore, at the applied stress, the minimum size of the PFZ can be calculated using the dislocation creep model and threshold stress, where the width of PFZ can be taken as the interparticle spacing.

This means that the minimum width of the PFZ would be an “inter particle spacing” that the threshold stress would be equal to the applied stress. In the case of the matrix of the FCA alloys, the minimum width of the PFZ is approximately 200 nm. However, the calculated strain rates below the experimentally observed strain rates may not be significant because the contribution is too small. Only until the calculated strain rates, for a particular width, reaches the observed strain rates will the PFZ contribute to creep. For the FCA alloys, this particular PFZ width is estimated to be approximately 400 nm. The measured PFZ for all alloys is more than 800 nm, and thus creep deformation should be partitioned to the PFZ. However, it remains unclear which feature is dominating, and there must be a relationship between the area fraction of Laves phase and the width of the PFZ.

The grain boundary region comprises two parameters, area fraction of Laves phase on the grain boundary and the width of the PFZ. It is possible to combine these parameters to create a factor which can be used to predict when failure is most likely to occur. Equation [3] describes a Grain Boundary Zone Strength Factor (GBZ SF). This factor essentially takes the ratio of the area fraction of Laves phase to the width of the PFZ.

$$\text{GBZ SF} = \frac{f_{\text{GB}}^{\text{Laves}}}{\delta_{\text{PFZ}}}, \quad [3]$$

where $f_{\text{GB}}^{\text{Laves}}$ is the area fraction of the Laves phase on the grain boundary and δ_{PFZ} is the width of the PFZ. Because this factor is related to both the area fraction of Laves phase and the width of the PFZ, the factor would be expected to change with time. This method allows for

Table III. Comparison of the Area Fraction of Laves Phase on the Grain Boundary and Width of PFZ After Creep Test in FCA-1Nb and FCA-2Nb Samples

At Fracture	$f_{\text{GB}}^{\text{Laves}}$	δ_{PFZ} (μm)
FCA-1Nb	0.487	0.813
FCA-2Nb	0.793	1.437

the tracking of the likeliness of failure. Figure 14 shows the creep curves of the FCA alloys. Overlaid on the curves are selected GBZ SF for the aging conditions of FCA-1Nb and FCA-2Nb and for the post creep rupture condition. All the creep-ruptured samples had a GBZ SF below 0.6. The calculated GBZ SF for the FCA-1Nb aged sample with 168 and 1008 hours of aging close to 0.6. This shows that the creep condition and aging conditions compare well. In this case the FCA-1Nb sample is already in a microstructural state that is susceptible to failure and it is not surprising that the sample failed quickly. The aging conditions for the FCA-2Nb sample showed a drastically different result. After aging for 168 hours the GBZ SF was calculated to be 1.14. If the assumed correlation between the aging and creep microstructure is accurate, it can be postulated that this value would have been similar during creep. Since the value was greater than 0.6, the conditions are not favorable for failure, thus the continuation of creep testing. After aging for 1008 hours the GBZ SF was calculated to be 0.8. This means that the areal fraction of Laves phase and the width of the PFZ is evolving, and is approaching conditions favorable for failure. Again, the GBZ SF was calculated for the gauge section after rupture in the FCA-2Nb sample. The value was calculated to be 0.58, which is below 0.6. Similarly, if the assumed aging to creep microstructure correlation is correct, then the observed values show an evolution with time and approach a condition favorable for failure.

The GBZ SF does not necessarily require there to be a direct relationship between the two parameters. Repeating the creep modeling of the PFZ from above, it was shown that dislocations move within the PFZ. This allows for deformation to occur exclusively adjacent to the grain boundary. In addition, it is also known that free grain boundaries are excellent sinks for defects.^[33,40,41] Therefore, any free amount of the grain boundary in the FCA alloy would be expected to form creep cavities. Any areal fraction of Laves phase less than 1.0, would have points on the grain boundary that is devoid of Laves phase particles. Both of the alloys, at failure, had an area fraction less than 0.8. It is not yet

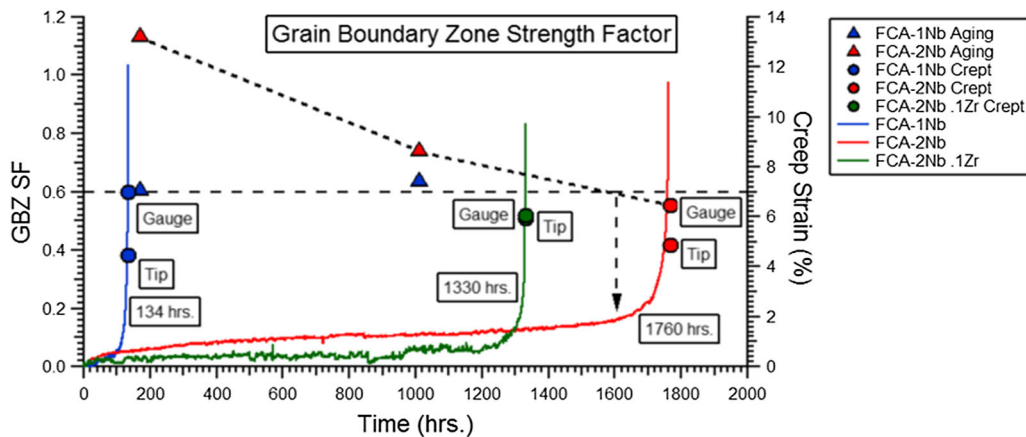


Fig. 14—Calculation of the GBZ SF overlaid onto the creep curves of the Fe-Cr-Al alloys. All the alloys failed when the GBZ SF drops below a value of 0.6.

known the relationship between the areal fraction of Laves phase and the width of the PFZ.

V. SUMMARY

Newly developed Fe-30Cr-3Al alloys with different Nb and Zr additions were creep tested and the global creep properties were determined and correlated to microstructure evolution. The creep-ruptured samples revealed a heterogeneous microstructure and there was a competition between the creep deformation in the matrix and the PFZ. With the results presented here, the FCA-2Nb alloy shows promise to fulfill the need of enhanced creep strength, with the added benefit of stable precipitates. Although welding on the alloy was not performed, the solutionization treatment appears to allow the alloys to be welded without precipitate interaction in the HAZ. The salient findings from this research are summarized below.

- (1) The FCA-1Nb sample did not contain Laves precipitates within the matrix prior to creep testing. The FCA-2Nb and FCA-2Nb-1Zr alloys contained Laves phase on the grain boundary and within the grain interior. Atom probe tomography revealed that the chemical composition of the Laves phase was close to the equilibrium composition and therefore the creep should be correlated to the coarsening rate.
- (2) The microstructures of the aging specimens at 973 K (700 °C) for both the FCA-1Nb and FCA-2Nb samples were similar. The size and density of the Laves phase particles were within the same order of magnitude for these two alloys. However, the creep rupture curves of these alloys indicated an order of magnitude difference, *i.e.*, the FCA-1Nb sample failed at 138 hours, whereas the FCA-2Nb sample failed at 1760 hours. The fractography indicates that the failure occurred at the grain boundaries in both FCA-1Nb and FCA-2Nb. Laves phase particles were found to be present in the ductile cups indicating cavities forming around them.
- (3) After creep rupture, the Laves phase particles in the gauge section and grain interior were different in size and number density (FCA-1 Nb: 93 nm, 1.88×10^{19} , FCA-2Nb: 138 nm, 1.15×10^{19}). TEM imaging revealed that in the grain interior the dislocations were pinned at the Laves phase. The dislocations in the PFZ were free to move. With the observation of creep voids on the grain boundaries and grain boundary cracking, the observed creep failure was attributed to a grain boundary failure mechanism.
- (4) A phenomenological model that described the creep deformation by dislocation and GBS was used to rationalize the data. The dislocation model indicated that the minimum creep rates for all the alloys should be very similar. However, the GBS model supported the observed creep failures. The uncertainties in these two models were discussed.

- (5) The experimental data pertaining to areal fraction of Laves phase and width of the (PFZ) showed a strong correlation to the creep rupture. The GBZ SF defined by the ratio of areal fraction of Laves phase on the grain boundary to the width of the PFZ, correlated well with the creep life. The data suggest that when the GBZ SF reached a critical value of 0.6 or below, rapid creep failure occurred.
- (6) Preferential creep deformation in the PFZ was tentatively supported by the crystallographic grain rotation and the amount of misorientation within the PFZ. For similar creep conditions, the grain interior did not show any significant orientation changes. The preferential deformation close to the grain boundary in PFZ and lack of deformation in grain interiors suggested a “core-and mantle” rotation mechanisms for the observed creep failures.

ACKNOWLEDGMENTS

The authors thank Dr. Xinghua Yu and Thomas Muth at Oak Ridge National Laboratory for their comments on this manuscript. Research sponsored by the Crosscutting Research Program, Office of Fossil Energy, U.S. Department of Energy. A portion of this research was conducted at the Center for Nanophase Materials Sciences, which is a DOE Office of Science User Facility.

REFERENCES

1. Environmental Protection Agency, *EPA 430-R-16-002*, Washington, DC, April 2016.
2. F. Abe: *Sci. Technol. Adv. Mater.*, 2008, vol. 9, p. 013002.
3. P. Auerkari, S. Holmström, J. Veivo, and J. Salonen: *Int. J. Pressure Vessels Pip.*, 2007, vol. 84, pp. 69–74.
4. H. Hirata and K. Ogawa: *Weld. Int.*, 2005, vol. 19, pp. 118–24.
5. H. Hirata and K. Ogawa: *Weld. Int.*, 2005, vol. 19, pp. 109–17.
6. K. Laha, K.S. Chandravathi, P. Parameswaran, and K. Bhanu Sankara Rao: *Metall. Mater. Trans. A*, 2008, vol. 40A, pp. 386–97.
7. S. Tsukamoto, M. Tabuch, T. Shirane and F. Abe, *Trends in Welding Research*, 2009, pp. 296–302.
8. Y. Yamamoto, X. Yu, S.S. Babu, and B. Shassere: *Proceeding of the 10th Liège Conference on Materials for Advanced Power Engineering*, 2014.
9. F. Abe: *Metall Mater Trans A*, 2005, vol. 36A, pp. 321–32.
10. M. Shibuya, Y. Toda, K. Sawada, H. Kushima, and K. Kimura: *Mater. Sci. Eng A*, 2011, vol. 528, pp. 5387–93.
11. B. Kuhn, C.A. Jimenez, L. Niewolak, T. Hüttel, T. Beck, H. Hattendorf, L. Singheiser, and W.J. Quadakkers: *Mater. Sci. Eng. A*, 2011, vol. 528, pp. 5888–99.
12. Y. Yamamoto, B.A. Pint, B. Shassere, and P.S.S. Babu: Oak Ridge National Laboratory (ORNL), Oak Ridge, TN, 2016.
13. Y.-T. Chiu and C.-K. Lin: *Journal of Power Sources*, 2012, vol. 198, pp. 149–57.
14. F. Abe, T.-U. Kern and R. Viswanathan, *Woodhead Publishing*, 2008.
15. ASTM_E8/E8M-16a, 2016.
16. ASTM_E139-11, 2016.
17. R.L. Coble: *J. Appl. Phys.*, 1963, vol. 34, pp. 1679–82.
18. I. Lifshitz: *Sov. Phys. JETP*, 1963, vol. 17, pp. 909–20.
19. D. Williams and B. Carter: Springer Science-Business Media, New York, 2009.

20. T.F. Kelly and M.K. Miller: *Rev. Sci. Instrum.*, 2007, vol. 78, p. 031101.
21. G. Li, N. Zhao, T. Liu, J. Li, C. He, C. Shi, E. Liu, and J. Sha: *Mater. Sci. Eng. A*, 2014, vol. 617, pp. 219–27.
22. N. Pourkia, M. Emamy, H. Farhangi, and S.H.S. Ebrahimi: *Mater. Sci. Eng. A*, 2010, vol. 527, pp. 5318–25.
23. B.L. Wu, G.Y. Sha, Y.N. Wang, Y.D. Zhang, and C. Esling: in *Materials science forum*, Trans Tech Publ, 2007, pp. 917–22.
24. F. Stein, G. Sauthoff, and M. Palm: *J. Phase Equilib.*, 2002, vol. 23, pp. 480–94.
25. A. Khvan and B. Hallstedt: *Calphad*, 2012, vol. 39, pp. 62–69.
26. T.D. Nguyen, K. Sawada, H. Kushima, M. Tabuchi, and K. Kimura: *Mater. Sci. Eng. A*, 2014, vol. 591, pp. 130–35.
27. J.A. Wert, E. Parker, and V. Zackay: *Metall. Mater. Trans. A*, 1979, vol. 10A, pp. 1313–22.
28. M.F. Ashby: *Acta Metall. Mater.*, 1966, vol. 14, p. 679.
29. K. Maruyama, K. Sawada, and J. Koike: *ISIJ Int.*, 2001, vol. 41, pp. 641–53.
30. M. Taneike, F. Abe, and K. Sawada: *Nature*, 2003, vol. 424, pp. 294–96.
31. J.E. Bird, A.K. Mukherjee, and J.E. Dorn: California Univ., Berkeley, Lawrence Radiation Lab., 1969.
32. M.F. Ashby: *Acta Metall. Mater.*, 1972, vol. 20, pp. 887–97.
33. T.G. Langdon and F.A. Mohamed: *J. Mater. Sci.*, 1978, vol. 13, pp. 1282–90.
34. F.A. Mohamed and T.G. Langdon: *Metall. Mater. Trans. A*, 1974, vol. 5A, pp. 2339–45.
35. B.A. Shassere, Y. Yamamoto, and S.S. Babu: *Metall. Mater. Trans. A*, 2016, vol. 47, pp. 2188–2200.
36. J. Wadsworth, O.A. Ruano, and O.D. Sherby: in *Minerals, Metal and Materials Society Annual Meeting, San Diego, Calif*, 1999.
37. T.G. Langdon: *Philos. Mag.*, 2006, vol. 22, pp. 689–700.
38. H. Lüthy, R.A. White, and O.D. Sherby: *Mater. Sci. Eng.*, 1979, vol. 39, pp. 211–16.
39. R.C. Gifkins: *Metall. Trans. A*, 1976, vol. 7A, pp. 1225–32.
40. L.-B. Niu, A. Katsuta, M. Kobayashi, and H. Takaku: *ISIJ Int*, 2003, vol. 43, pp. 251–55.
41. X.J. Wu and A.K. Koul: *Metall. Mater. Trans. A*, 1995, vol. 26A, pp. 905–14.